RSC Advances

PAPER

Cite this: *RSC Adv.*, 2014, **4**, 44004

Theoretical studies of geometry asymmetry in tellurium nanostructures: intrinsic dipole, charge separation, and semiconductor–metal transition

Yan-Mei Tan,[a] Yu-Jun Zhao,[ab] Lin-Bao Luo,[c] Xiao-Bao Yang*[ab] and Hu Xu*[d]

Received 27th May 2014
Accepted 4th September 2014

DOI: 10.1039/c4ra04988h

www.rsc.org/advances

Bulk tellurium (Te) presents a threefold screw axis with highly anisotropic chain structure, where every Te atom forms strong covalent bonds in the chain and much weaker bonds in the adjacent chains. The bonds in the adjacent chains are critical to the total energies of Te nanostructures since the nearest neighbors are always saturated. Confirmed by our model simulation and first-principles calculations, the *nanobelts* would be stabilized at the temperature of 600 K due to the entropy effect, though the hexagonal nanowires have the smallest surface-to-volume ratio. Attributed to the geometry asymmetry of the highly anisotropic chain, we showed that the difference of weaker bonds' distribution induces an intrinsic dipole, and thus a charge separation at the two ends of Te nanobelts. Interestingly, it further leads to a semiconductor–metal transition which is also verified by our first-principles calculations. Our finding provides a new mechanism of charge separation and semiconductor–metal transition, due to the unique asymmetry of geometry in Te nanostructures.

I. Introduction

Recently, one-dimensional (1-D) nanostructures[1,2] have received increasing research interest due to their novel properties and potential applications as promising building blocks in various nano-devices.[3–5] For example, due to their tunable electronic and optical properties, 1-D semiconductor materials[6–10] have been widely used in optoelectronic devices including light emitting diodes (LEDs), ultraviolet light (UV) photodetectors, and memory devices. In addition, 1-D semiconductor nanostructures, especially the coaxial core/shell hetero-nanostructures can also be used as solar cells which are characterized by efficient separation of photon-generated electron–hole pairs.[11] While commercial production of photovoltaic devices (PV) is known to be largely limited by high cost and suffers from low efficiency, it is highly desirable to open up a new avenue for charge separation in designing solar cells with high efficiency and low cost.

Bulk tellurium (Te) is a small gap semiconductor and presents a threefold screw axis with highly anisotropic chain structure,[12–14] whose electronic structure has been investigated by various experimental studies[15,16] and a group of theoretical treatments.[17–21] Compared with its thin film and bulk counterparts, 1-D Te nanostructure has been reported to show distinct size-dependent properties. These features render it a promising candidate for possible applications in PV devices.[22] Normally, 1-D Te nanostructures with hexagonal cross-sections are known to be the most stable,[20] and the band gap and optical conductivity of nanowires (NWs) were both size- and shape-dependent.[21] Recently, we found that the surface of silicon (Si) NWs with dangling bonds[23] as well as 1-D Se nanobelts (NBs) with hydrogen adsorption[24] could provide acceptor levels to trap electrons and induce p-type conduction, which could be further modulated by molecular adsorption. However, few theoretical efforts have been made in Te NBs, in spite of its facile synthesis and practical applications according to our experimental progress.

In most PV devices, p–n junctions are one of the most indispensable components to realize charge separation. However, charge separation has also been demonstrated in various systems without volume doping.[25–30] By the control of morphology, the highest-occupied state and the lowest-unoccupied state could be separated along the wire axis in tapered Si NWs.[25] Similar phenomenon was observed in Si NWs under partial strain along the wire axis,[26] as well as Si quantum dots[30] and ZnO NWs[27] with surface reconstructions. In addition, the natural charge spatial separation behaviors exhibit in the coaxial core/shell hetero-nanostructures, such as Si-core/Ge-shell NWs[28] and ZnO-core/GaN-shell NWs.[29] In these systems, there is asymmetrical distribution of electrostatic potential due to the geometry asymmetry, which would simultaneously

[a]*Department of Physics, South China University of Technology, Guangzhou 510640, P. R. China. E-mail: scxbyang@scut.edu.cn*

[b]*Key Laboratory of Advanced Energy Storage Materials of Guangdong Province, P. R. China*

[c]*School of Electronic Science and Applied Physics, Hefei University of Technology, Hefei, Anhui 230009, P. R. China*

[d]*Department of Physics, South University of Science and Technology of China, Shenzhen, P. R. China. E-mail: xu.h@sustc.edu.cn*

produce internal electric field and finally induce charge separation. Enlightened by these work, we expect that Te nanostructures are probably capable of separating carriers, considering the highly anisotropic chain structure and novel geometry asymmetry.

In this paper, we systematically studied the structural stabilities of 1-D Te nanostructures, focusing on the geometry asymmetry's effect on their electronic properties. Considering both Te NWs and NBs with various shapes and sizes, we show that hexagonal Te NWs are most stable while Te NBs would be stabilized due to the entropy's contribution as the temperature increases. Remarkably, the geometry symmetry would cause the charge separation of valence bands and conduction bands in Te NBs, which might further induce the semiconductor–metal transitions. The electronic properties of Te nanostructures were found to be dominated by the intrinsic dipole, which can be easily estimated by our model analysis.

II. Computational methods

The first-principles calculations of both Te NWs and NBs were based on the density functional theory (DFT) implemented in the Vienna *ab initio* simulation package method.[31,32] The projector augmented wave (PAW) and the Perdew–Burke–Ernzerh of GGA (PBE) functional[33,34] were employed for the total energies calculations. The energy cutoff was 200 eV and the criteria of the forces was set to be 0.01 eV Å^{-1} for all atoms. Various values of energy cutoff from 200 eV to 500 eV were test and the energy difference per atom was found to be within 0.15 meV. A mesh of $1 \times 1 \times 5$ of k-point grid was used in the relaxation and it was increased to $1 \times 1 \times 10$ for the band structure calculations. To avoid the cell-to-cell interactions, the vacuum distance was carefully test and the Neugebauer–Scheffler dipole correction was also applied.[35] For higher accuracy of total energies, we have considered the dispersion correction.[36] In addition, we have applied the G_0W_0 approximation the band gap correction.[37]

To estimate the entropy's contribution, we adopted the bond energy model to calculate the total energies (E) and simulated the density of states $g(E)$, using the Wang–Landau algorithm.[38] The probabilities $p(E)$ of Te nanostructures as a function of temperature (T) were calculated as $p(E) = g(E)\exp(-\beta E)/Z$, where the partition function $Z = \sum_E g(E)\exp(-\beta E)$ and $\beta = 1/k_BT$. The structural stabilities under given temperature were determined by the probability $p(E)$, which would depend on both the total energies and density of states.

III. Results and discussions

As shown in Fig. 1, bulk Te consists of long parallel helical chains arranged in a triangular system, in which there are two nearest neighbors in the chain and four next nearest neighbors in the adjacent chains. We considered 1-D Te nanostructures with various shapes of cross-sections, including triangular, quadrilateral, hexagonal NWs and NBs with various aspect ratios (width/thickness). Note that we focused on three typical

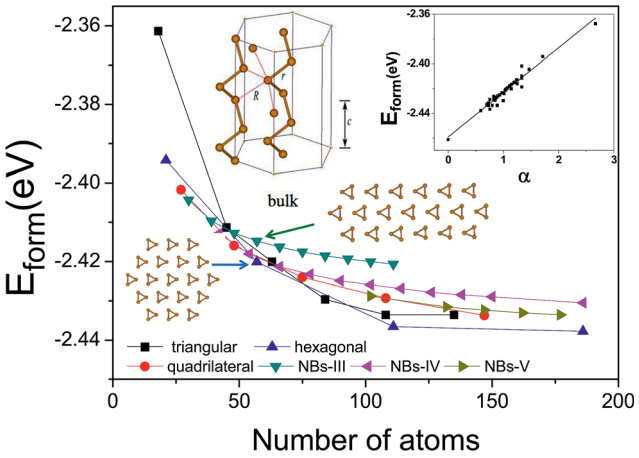

Fig. 1 The formation energies of Te NWs and Te NBs as a function of shape and size, obtained from the first-principles calculations. In bulk Te, the nearest neighbors in the chain and the next nearest neighbors in the adjacent chains are marked with the bond length of r and R, respectively. The structures of hexagonal NWs and NBs-III containing 57 Te atoms per unit cell are shown as an example. The inset shows the formation energies of Te NWs and Te NBs as a function of α.

kinds of NBs (NBs-III, NBs-IV, NBs-V) with the thicknesses of 7.8 Å, 11.9 Å, and 15.6 Å respectively, containing three, four and five chain structures along the y direction correspondingly. For every kind of NBs, the aspect ratio of NBs was allowed to vary as a function of the width. A structure of hexagonal NWs containing 57 Te atoms per unit cell is shown as an example, as well as the corresponding one of NBs-III.

A. Thermodynamic stabilities

To determine the structural stabilities, we defined the formation energy (E_{form}) as the difference of the total energies per Te atom in the nanostructures and a gas state, *i.e.* the structure with lower E_{form} is more stable. Fig. 1 shows the calculated E_{form} of Te nanostructures as a function of shape and size, in which an inverse relation between the formation energy and size was observed, indicating the nanostructures are progressively more stable as the size increases. Moreover, for a certain size, the formation energy is also shape-dependent, implying that the stability of the Te nanostructures is affected by the cross-section. The hexagonal ones were further found to be the most stable, in agreement with previous studies.[20] The structural stability dependence on the size is much more significant for small NWs and NBs, while the formation energies of NWs and NBs approach to the one of bulk Te as the size gradually increases.

Similar to our previous studies,[30,39,40] we described the structural stabilities with the bond energies. In bulk structure, every Te atom forms strong covalent bonds with the two nearest neighbors in the chain and much weaker bonds with the four next-nearest (NN) neighbors in the adjacent chains. Thus, the formation energy (E_{form}) per Te atom in the Te nanostructures can be calculated by $E_{form} = -E_{Te-Te} - 2E_{Te-Te}' + 0.5\alpha E_{Te-Te}'$, where E_{Te-Te} and E_{Te-Te}' are the bond energies of nearest and

NN neighboring Te–Te bonds, respectively, α is the ratio of the number of missing NN neighboring bonds to the number of Te atom. As shown in the inset of Fig. 1, the formation energy of Te nanostructures is consistent with a linear dependence on α, and approaches the value in bulk structure as α reaches zero. In light of this, hexagonal NWs are more stable since there are less missing bonds and smaller surface-to-volume ratio.

For comparison, we also considered the effect of dispersion correction. The lattice constants of bulk Te along a, c axis are 4.62 Å and 5.98 Å respectively with the cohesive energy of −2.27 eV per atom, which is in agreement with the previous calculations and experimental measurement.[41,42] For the hexagonal NWs and NBs-III with 57 atoms per unit cell, Te NWs is found to be more stable than NBs by 0.0053 eV per atom according to the DFT calculation without dispersion correction. After applying the dispersion correction, the energy difference is increased to be 0.015 eV. Thus, the trend of structural stabilities for Te nanostructures from DFT calculations is reliable.

B. Temperature effect

According to the experimental results, Te NBs were synthesized around 600 K, with energies higher than hexagonal NWs. Note that the difference of formation energies of Te nanostructures is originated from the weak interactions between Te atoms and their NN neighbors, affecting the formation energies in the order of 10 meV, which would decrease to around 5 meV as the NBs' thickness increase (shown in Fig. 1). Thus, we considered the temperature effect on the structural stabilities of Te nanostructures, by estimating the entropy's contribution through the Wang–Landau algorithm. To simulate the density of states $g(E)$, we adopted the bond energy model to estimate the total energies (E) and the probabilities of $p(E)$ for given Te nanostructures according to the Boltzmann distribution, where $E = NE_{\text{form}} + NE_{\text{atom}} = N(-E_{\text{Te–Te}} - 2E_{\text{Te–Te}}' + 0.5\alpha E_{\text{Te–Te}}' + E_{\text{atom}})$, E_{atom} is the isolated energy of Te atom and N is the number of Te atoms per unit cell. The structure is more stable with higher probability $p(E)$.

Fig. 2(a) shows the probabilities $p(E)$ of Te nanostructures with various cross-sections as a function of temperature, containing 57 Te atoms per unit cell. The inset shows the dependence of logarithm of $g(E)$ on the number of NN Te–Te bonds, which corresponds to the formation energy of a given structure. As the temperature increases, the structures with less NN bonds become more stable. The number of NN bonds for the most probable structure is 84 and 82 at T = 200 K and 400 K respectively, while it remains 80 when the temperature is from 600–800 K. Note that the hexagonal structure with 84 NN bonds is unique, while there are many isomers for the structures with 80 NN bonds.

As shown in Fig. 2(b), there are two typical structures with 80 NN bonds and the structure (S_2) of NBs-III is of higher E_{form} than that of the S_5 structure, with 57 Te atoms per unit cell (19 Te chains). We also considered the possible transitional structures (S_1 and S_3) for S_2, containing 54 and 60 Te atoms (18 and 20 Te chains) respectively. For example, we removed one Te chain from S_2 at various positions and obtained the most

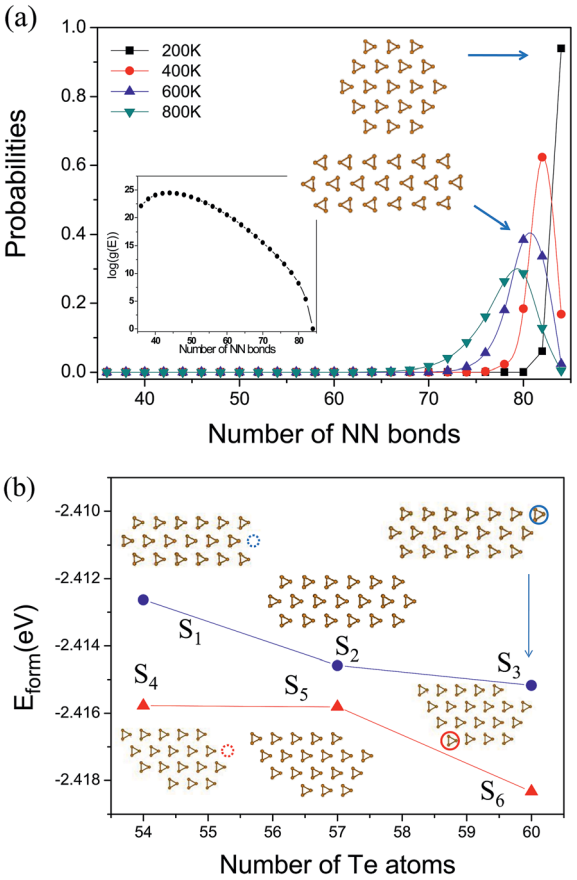

Fig. 2 (a) The probabilities of Te nanostructures with 57 atoms per unit cell as a function of temperature; (b) the formation energies of possible transitional Te nanostructures with 54, 57 and 60 atoms per unit cell. The circles in dashed and solid lines are marked for the removing and adding Te chains.

stable one of S_1, adding one Te chain to form the S_3 structure. It found that S_2 would be stable by the analysis of convex hull,[30] since $2E_{\text{form}}(S_2) < E_{\text{form}}(S_1) + E_{\text{form}}(S_3)$. Thus, we could understand the appearance of NBs-III as follows: (1) the hexagonal NW is destabilized as the temperature increases, and the structures with less NN bonds and high $g(E)$ become more stable; (2) the structure of NBs-III possesses local minimum of E_{form} and remains stable without transitioning into other structures with different number of Te atoms.

Similar operations were applied to the S_5 structure, obtaining the S_4 and S_6 structures. According to the analysis of convex hull, the S_5 structure should not appear though it is of lower E_{form} than that of S_2. As shown in Fig. 2(b), the transition of S4 and S6 from S_5 is preferable. During the formation of Te nanostructures, the atoms' number of irregular structures such as S_5 would be deviated from 57, while the regular structure of NBs-III would remain stable and probably observed in experiments.

C. Charge separation

Te nanostructures exhibit significant geometry asymmetry due to highly anisotropic chain structure, which is expected to affect

the charge distributions greatly. Thus, we investigated the charge distribution of valence band maximum (VBM) and the conduction band minimum (CBM) for Te nanostructures, including triangular, quadrilateral, hexagonal NWs and NBs-III, NBs-IV, NBs-V. In these Te nanostructures, every Te atom has two nearest neighbors and the systems exhibit various symmetries, due to the number of the next nearest neighbors around surface (shown in Fig. 3(a)). Triangular and hexagonal NWs present the property of C_{3v} symmetry, while quadrilateral NWs and NBs (III, V) are symmetric about the x-axis.

Fig. 3(a) shows the charge spatial distribution of NWs and NBs for the bands near the Fermi level. We note that the spatial distribution of VBM and CBM in triangular and hexagonal NWs has the symmetry of C_{3v}, while it is axial symmetry in quadrilateral NWs, which indicates the consistency of charge distribution of NWs depends on the structural symmetry. For triangular cross section, the VBM states are mainly localized in the core section, whereas the CBM states are mainly distributed in the shell section. For the quadrilateral wires, the VBM and CBM are distributed on the two ends, respectively. For NBs structures, the charge separation of the CBM and VBM is also evident. Interestingly, the charge distribution of the three kinds of NBs structures displays a similar behavior with their VBM and CBM located in different ends of NBs. Furthermore, the charge spatial separation of Te NBs has axial symmetry along the x axis and it is determined by the structure symmetry. In other words, Te NBs can keep holes and electrons in the opposite segments, and be capable of separating the charge carriers intrinsically. Notably, this carrier separation ability can be easily modulated by the geometry asymmetry of surface structures.

In general, the asymmetrical distribution of electrostatic potential would induce charge separation. As shown in Fig. 3(b), when there is no polarization and the electrostatic potential is distributed uniformly, the charge distributions of VBM and CBM are spatially uniform. The energy levels would bend with the electrostatic potential when there is a polarization field, which induces the spatial separation of VBM and CBM. In order to reveal the mechanism responsible for the charge separation and the intrinsic dipole, we have systematically analyzed the structural characteristics of Te nanostructures, taking NBs-III with 57 atoms in a unit cell as an example. From the Fig. 3(b), the number of missing NN neighbors for surface atoms depends on the position, which maintains the axis symmetry along the x direction. In each helical chain, there are more electrons located at Te atoms with the less number of missing NN neighbors, which would produce a dipole. Neglecting the charge transfer between the chains, the dipole of the j-th chain can be calculated as $\boldsymbol{p}_j = \sum_{i=1}^{3} \boldsymbol{p}_{ij} = q_{ij}\boldsymbol{r}_{ij}$, where q_{ij} and $\boldsymbol{r}_{ij}$ stand for the effective charge and the vector from the Te atom to the chain axis. In our model, we only focus on the dipole direction and assume that the effective charge should be proportional to the difference between the next neighboring number of Te atom and the average number of next neighbors in the helical chain. Thus, the total dipole $\boldsymbol{P}$ can be calculated as $\boldsymbol{P} = \sum_{j=1}^{n} \boldsymbol{p}_j$, for a Te nanostructures containing n helical chains. Fig. 3(b) shows the dipole distribution of the NBs-III obtained in our model analysis. Note that the dipoles at the two ends of NBs are of same strength and opposite directions, while the dipoles on the surface produce net components along the x direction. As a result, the total dipole is from left to right, inducing an electric field pointing to the left segment.

Fig. 3(c) shows the dipole moment of NBs-III as a function of size obtained by the first-principles calculations, with the results from the model prediction shown in the inset for comparison. When we determine the direction of the total dipole in our model, we initially neglect the charge transfer between the chains, and thus there is a linear dependence of the dipole moment on the size of NBs. According to the first-principles results of NBs-III, however, the dipole moment increases almost linearly at the beginning and then approach to the maximum gradually. The deviation from linear changes of the dipole moment is mostly ascribed to the fact that the charge transfer between the chains could not be neglected as the dipole moment increases. In addition, the relaxation of atoms would also reduce the dipole moment. Though the practical charge transfer and atom relaxations would reduce the dipole to a certain extent, it will not reverse the direction of the dipole. Thus, the charge distributions of VBM and CBM are mainly distributed at the left and right ends of NBs respectively, as is verified by the first-principles calculations. In our model, the effective charge is assumed to be dependent on the number of the NN neighboring bonds and the values of dipole moment should be qualitative (using arbitrary unit, a.u., for simplicity). The dipole moment in our model prediction could be helpful for the understanding of Te nanostructures' electronic properties, such as charge separation and semiconductor–metal transitions.

In tapered Si nanostructures,[25] the spatial distributions of highest-occupied states are mostly localized in the narrowest part, with lowest-unoccupied states in the widest parts. For comparison, we considered two NBs structures of uneven thicknesses along the x direction (shown in Fig. 3(c)). According to our model analysis, the dipoles of both NBs structures are pointing to the right region, which should induce a similar charge separation as the NBs-III. From the results of the first-principles calculations, the charge distribution of VBM is mainly distributed at the left end with the CBM at the right, indicating no dependence on the thickness. Thus, the separation of charge carriers of Te nanostructure is attributed to the intrinsic dipole resulting from the geometry asymmetry.

D. Semiconductor–metal transitions

According to the model analysis, the dipole would not only induce the charge separation of VBM and CBM, but also cause the bands bending which might reduce the band gaps. We shows the calculated band gaps of Te NWs and NBs as a function of the sizes and cross-sections in Fig. 4(a), where the one in bulk Te (0.14 eV) is indicated by the dotted line for comparison.

Due to the quantum confinement, the band gap dependence on the diameter becomes more significant for small wires, inducing larger band gaps than the bulk one. In the large size regime, the band gap decreases gradually as the size of NWs increases further, approaching to that of bulk Te. For the triangular NWs, the gap value is 1.06 eV when the diameter is 9 Å, while it is 0.62 eV for a diameter of 36 Å. Similarly, the band gaps of hexagonal/quadrilateral NWs decrease from 0.72/0.80 eV to 0.46/0.48 eV when the size increases. Note that the decrease of band gaps of quadrilateral NWs is more significant, compared to the hexagonal ones.

For the possible application for solar cell, the materials should have a band gap about 1.5 eV. The experimental value of band gap for bulk Te is 0.33 eV while it is only 0.14 eV from DFT, since the band gaps are always underestimated by DFT calculations. We have performed the G_0W_0 calculation and the band gap is found to be 0.38 eV, in agreement with the experimental value. For the Te NBs with 57 atoms per unit cell, the band gap from DFT is 0.32 eV and it is 1.08 eV from the G_0W_0 calculation. Thus, for the Te nanostructures with the band gaps around 0.6–0.8 eV from DFT, the experimental values should be around 1.2–2.4 eV, which is suitable for the application of solar cell.

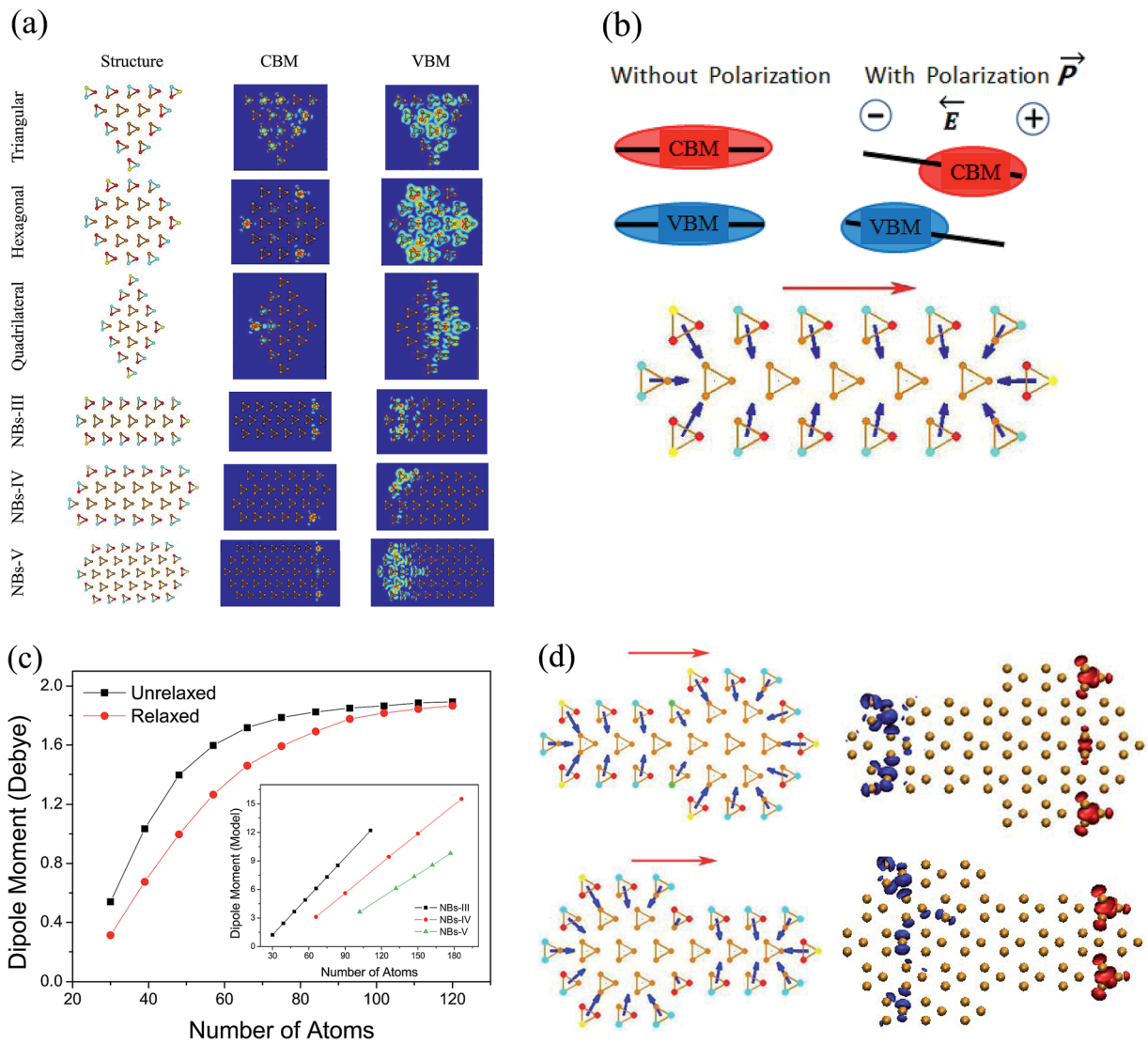

Fig. 3 (a)The geometry asymmetry and charge distribution of VBM and CBM in Te nanostructures. The brown spheres represent Te atoms with four next neighbors as in the bulk, while yellow, blue and red spheres represent Te atoms with missing four, three, and one next neighbors, respectively. The values are normalized into the interval of [0, 1] and represented by various color from blue to red. (b) The polarized field and the dipole moment of Te NBs. Taking the NBs-III with 57 atoms in the cross-section as an example, the dipole moment and direction of every Te chain is shown, and the red arrow indicates the total dipole direction. (c) The dipole moment of NBs-III as a function of size obtained by the first-principles calculations. The red circles and black squares represent the results with and without relaxations. The inset shows the results from model prediction for comparison. (d) The dipole moment and charge separation in Te nanostructures. Green spheres represent Te atoms with missing two next neighbors. We show the charge distributions for the states near the Fermi level, with VBM and CBM represented by blue and red, respectively.

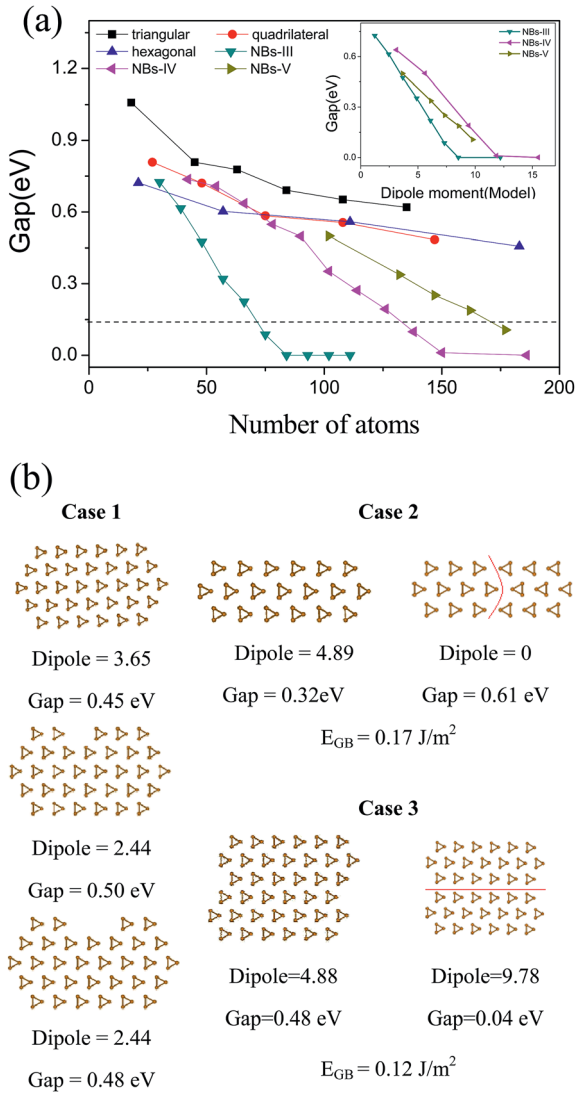

Fig. 4 The band gaps and dipole moments of Te nanostructures. (a) The gap values of Te NWs and NBs as function of size. The inset shows the dependence of band gap on the dipole moment. (b) Three more examples for the relationship between the band gap and the dipole moment.

As verified above, there is evident charge separation in various NBs due to the intrinsic dipole. As shown in Fig. 4(a), there is a dramatic decrease of band gaps as the width of NBs increases. The gaps are even lower than that of bulk Te when the aspect ratio reaches more than 4.62, 4.18 and 3.46 for the NBs-III, NBs-IV and NBs-V, respectively. As the width increases, all these three kinds of NBs would undergo a semiconductor–metal transition. For the NBs-III, the dipole moments mainly depend on the surface atoms which produce net components along the x direction. As show in the inset of Fig. 4(a), the gap of NBs decreases as the dipole moment increases, approaching zero and inducing the semiconductor–metal transitions. Before the transition, there is a linear dependence of gaps on the dipole moment.

Fig. 4(b) shows three more examples for the relationship between the band gap and the dipole moment. For the NBs–V, the band gap is 0.45 eV and the dipole moment is 3.65 a.u. When there are one or two missing Te chains on the side surface, the dipole moments would not change, resulting in little difference of band gaps (in case 1). The band gap of a NBs-III structure is 0.32 eV with the dipole moment of 4.88 a.u. (in case 2), while the dipole moment is almost zero when there is a grain boundary along the red line, with the right part of structure is inversed as a mirror image. In such a case, the gap would increase to 0.61 eV. In addition, we considered two nanostructures formed by different packing of the structure with the gap of 0.32 eV in case 2, which would produce the dipole moments of 4.88 a.u. and 9.78 a.u. respectively (in case 3). The structure on the left is a common NBs with the gap of 0.48 eV, while there is a grain boundary along the red line in the right one, with the band gap of only 0.04 eV which is far less than that of bulk material. The formation energies (E_{GB}) of grain boundary in case 2 and 3 are calculated to be 0.17 and 0.12 J m^{-2}, respectively. In polycrystalline silicon,[43] E_{GB} is over 0.5 J m^{-2} and the grain boundary in Te nanostructures should be also probable. Therefore, the band gap of Te nanostructures is dominated by the dipole moment, attributed to the geometry asymmetry and possible grain boundaries.

IV. Conclusion

In summary, we theoretically investigated the structural stabilities and electronic properties of Te nanostructures with various sizes and shapes. Compared with the hexagonal NWs, Te NBs are less stable with a higher surface-to-volume ratio, which could be stabilized due to the entropy contribution. Notably, there is evident charge separation of VBM and CBM in NBs due to the geometry asymmetry, which would also induce the dramatic decrease of band gaps. We demonstrated a new mechanism of modulating the electronic properties by the geometry asymmetry, which indicates a new approach for the design and fabrication of photovoltaic devices.

Acknowledgements

This work was supported by NSFC (Grant no. 11104080, 21101051), the Fundamental Research Funds for the Central Universities (2013ZZ0082, 2013HGCH0012), and KLGHEI (KLB11003). The computing resources from the HPC Lab, Shenzhen Institute of Advanced Technology, Chinese Academy of Sciences (CAS), and from Sc-Grid of the Supercomputing Center, Computer Network Information Center of CAS, are gratefully acknowledged.

References

1 A. M. Morales and C. M. Lieber, *Science*, 1998, **279**, 208.
2 Y. N. Xia, P. D. Yang, Y. G. Sun, Y. Y. Wu, B. Mayers, B. Gates, Y. D. Yin, F. Kim and Y. Q. Yan, *Adv. Mater.*, 2003, **15**, 353.
3 M. H. Huang, S. Mao, H. Feick, H. Q. Yan, Y. Y. Wu, H. Kind, E. Weber, R. Russo and P. D. Yang, *Science*, 2001, **292**, 1897.

4 Y. Cui and C. M. Lieber, *Science*, 2001, **291**, 851.
5 C. M. Lieber and Z. L. Wang, *MRS Bull.*, 2007, **32**, 99.
6 Y. Zhang, L. W. Wang and A. Mascarenhas, *Nano Lett.*, 2007, **7**, 1264.
7 E. C. Garnett and P. D. Yang, *J. Am. Chem. Soc.*, 2009, **130**, 9224.
8 B. Tian, T. J. Kempa and C. M. Lieber, *Chem. Soc. Rev.*, 2009, **38**, 16.
9 A. Nduwimana and X. Q. Wang, *Nano Lett.*, 2009, **9**, 283.
10 Y. Kanai, Z. G. Wu and J. C. Grossman, *J. Mater. Chem.*, 2010, **20**, 1053.
11 B. Z. Tian, X. L. Zheng, T. J. Kempa, Y. Fang, N. F. Yu, G. H. Yu, J. L. Huang and C. M. Lieber, *Nature*, 2007, **449**, 885.
12 R. H. Asendorf, *J. Chem. Phys.*, 1957, **27**, 11.
13 T. Starkloff and J. D. Joannopoulos, *Phys. Rev. B: Condens. Matter Mater. Phys.*, 1979, **19**, 1077.
14 J. R. Reitz, *Phys. Rev.*, 1957, **105**, 1233.
15 L. D. Laude, B. Kramer and K. Maschke, *Phys. Rev. B: Solid State*, 1973, **8**, 5794.
16 M. Wautelet and L. D. Laude, *Phys. Rev. Lett.*, 1977, **38**, 40.
17 J. D. Joannopoulos, M. Schluter and M. L. Cohen, *Phys. Rev. B: Solid State*, 1975, **11**, 2186.
18 A. Coker, T. Lee and T. P. Das, *Phys. Rev. B: Condens. Matter Mater. Phys.*, 1980, **22**, 2968.
19 G. Kresse, J. Furthmuller and J. Hafner, *Phys. Rev. B: Condens. Matter Mater. Phys.*, 1994, **50**, 13181.
20 J. Yang and W. Q. Zhang, *Acta Phys. Sin.*, 2007, **56**, 4017.
21 P. Ghosh, M. U. Kahaly and U. V. Waghmare, *Phys. Rev. B: Condens. Matter Mater. Phys.*, 2007, **75**, 245437.
22 L. B. Luo, F. X. Liang, X. L. Huang, T. X. Yan, J. G. Hu, Y. Q. Yu, C. Y. Wu, L. Wang, Z. F. Zhu, Q. Li and J. S. Jie, *J. Nanopart. Res.*, 2012, **14**, 967.
23 L. B. Luo, X. B. Yang, F. X. Liang, H. Xu, Y. Zhao, X. Xie, W. F. Zhang and S. T. Lee, *J. Phys. Chem. C*, 2011, **115**, 18453.
24 L. B. Luo, X. B. Yang, F. X. Liang, J. S. Jie, Q. Li, Z. F. Zhu, C. Y. Wu, Y. Q. Yu and L. Wang, *CrystEngComm*, 2012, **14**, 1942.
25 Z. G. Wu, J. B. Neaton and J. C. Grossman, *Phys. Rev. Lett.*, 2008, **100**, 246804.
26 Z. G. Wu, J. B. Neaton and J. C. Grossman, *Nano Lett.*, 2009, **9**, 2418.
27 L. Z. Kou, C. Li, Z. Y. Zhang, C. F. Chen and W. L. Guo, *Appl. Phys. Lett.*, 2010, **97**, 053104.
28 M. Amato, M. Palummo and S. Ossicini, *Phys. Rev. B: Condens. Matter Mater. Phys.*, 2009, **80**, 235333.
29 Z. H. Wang, Y. C. Fan and M. W. Zhao, *J. Appl. Phys.*, 2010, **108**, 123707.
30 H. D. Lu, Y.-J. Zhao, X.-B. Yang and H. Xu, *Phys. Rev. B: Condens. Matter Mater. Phys.*, 2012, **86**, 085440.
31 G. Kresse and J. Furthmüller, *Phys. Rev. B: Solid State*, 1996, **54**, 11169.
32 G. Kresse and D. Joubert, *Phys. Rev. B: Condens. Matter Mater. Phys.*, 1999, **59**, 1758.
33 J. P. Perdew, K. Burke and M. Ernzerhof, *Phys. Rev. Lett.*, 1996, **77**, 3865.
34 J. P. Perdew, K. Burke and M. Ernzerhof, *Phys. Rev. Lett.*, 1998, **80**, 891.
35 J. Neugebauer and M. Scheffler, *Phys. Rev. B: Condens. Matter Mater. Phys.*, 1992, **46**, 16067.
36 S. Grimme, *J. Comput. Chem.*, 2006, **27**, 1787.
37 M. Shishkin and G. Kresse, *Phys. Rev. B: Condens. Matter Mater. Phys.*, 2007, **75**, 235102.
38 F. Wang and D. P. Landau, *Phys. Rev. Lett.*, 2001, **86**, 2050.
39 H. Xu, X. B. Yang, C. S. Guo and R. Q. Zhang, *Appl. Phys. Lett.*, 2009, **95**, 953106.
40 X. B. Yang, Y.-J. Zhao, H. Xu and B. I. Yakobson, *Phys. Rev. B: Condens. Matter Mater. Phys.*, 2011, **83**, 205314.
41 D. K. Ward, X. W. Zhou, B. M. Wong, F. P. Doty and J. A. Zimmerman, *Phys. Rev. B: Condens. Matter Mater. Phys.*, 2012, **85**, 115206.
42 X. W. Zhou, D. K. Ward, B. M. Wong and F. P. Doty, *Phys. Rev. Lett.*, 2012, **108**, 115206.
43 J. Zhang, C.-Z. Wang and K.-M. Ho, *Phys. Rev. B: Condens. Matter Mater. Phys.*, 2009, **80**, 174102.